Improved pseudopotential transferability for magnetic and electronic properties of binary manganese oxides from DFT+U+J calculations

Jin Soo Lim, Diomedes Saldana-Greco, and Andrew M. Rappe
The Makineni Theoretical Laboratories, Department of Chemistry, University of Pennsylvania, Philadelphia, Pennsylvania 19104-6323, USA
(Received 25 May 2016; revised manuscript received 6 September 2016; published 21 October 2016)

We employ the fully anisotropic DFT+U+J approach with the PBEsol functional to investigate ground-state magnetic and electronic properties of bulk binary manganese oxides: MnO, Mn_3O_4, α-Mn_2O_3, and β-MnO_2, in order of increasing Mn valence. The computed crystal structures, noncollinear magnetic ground states, and corresponding electronic structures are in good agreement with the experimental data and hybrid functional calculations available in the literature. We take into account the nonlinear core-valence interaction in our Mn pseudopotential designed by ourselves, as it has been proven to be important for transition-metal systems. Although the Hubbard U term is capable by itself of opening a band gap, the explicitly defined exchange parameter J plays an important role in improving the detailed electronic and noncollinear magnetic structure profiles. Appropriate band gaps are obtained with U values smaller than those used in previously reported calculations. Our results suggest that pseudopotential design together with DFT+U+J enables the acquisition of accurate properties of complex magnetic systems using a nonhybrid density functional.

DOI: 10.1103/PhysRevB.94.165151

I. INTRODUCTION

Due to the low cost, low toxicity, and high chemical stability, binary manganese oxides have a wide range of applications, such as catalysis [1], batteries [2,3], functional magnetic and optical materials [4,5], and electrocatalytic biosensors [6]. From a theoretical perspective, manganese oxides attract great interest due to their strong electron correlations that give rise to complex physical phenomena, including colossal magnetoresistance, charge and orbital ordering, and noncollinear magnetism. Although manganese oxides have been studied extensively, modeling their ground-state magnetic and electronic properties for different oxidation states within density functional theory (DFT) poses fundamental challenges, due to the inherent limitations in the approximations of the exchange-correlation functional. Improvements to these simulations without resorting to higher-level methods and incurring significant computational costs are therefore desirable for large-scale studies of systems involving strongly correlated materials. Here, we construct a pseudopotential that accounts for nonlinear core-valence interactions, and we apply the fully anisotropic DFT+U+J method. This approach accurately describes the magnetic and electronic properties of bulk manganese oxides with a variety of atomic and magnetic structures and different oxidation states, namely MnO, Mn_3O_4, α-Mn_2O_3, and β-MnO_2.

MnO exists in a $B1$ rock salt structure with Mn^{2+} oxidation state [Fig. 1(a)]. It undergoes a paramagnetic to type-II antiferromagnetic (AFM-II) transition at $T_N = 116$ K, accompanied by cubic ($Fm\bar{3}m$) to rhombohedral structural transition [7]. The ground-state magnetic structure AFM-II consists of ferromagnetically aligned planes that are successively antiparallel along the [111] direction. Consequent magnetostriction causes rhombohedral contraction along the [111] below T_N, tilting the crystal axes 0.62° from the cubic directions [8,9]. MnO is a charge-transfer insulator with a large band gap of 3.6–4.2 eV measured experimentally [10,11]. The electronic structure has been studied extensively via first-principles methods, including Hartree-Fock [12–17], LDA [14,18–20], GGA+U [15–18,20–23], the GW method [24], and hybrid functionals [15–17,21,25].

Mn_3O_4 exists in a spinel structure (AB_2O_4), with Mn^{2+} (Mn_A) occupying the tetrahedral sites (numbered Mn1–2) and Mn^{3+} (Mn_B) occupying the octahedral sites (numbered Mn3–6) [Fig. 1(b)]. Edge-sharing Mn_BO_6 octahedra form chains along $\boldsymbol{a}$ and $\boldsymbol{b}$. They undergo a cubic ($Fd\bar{3}m$) to tetragonal ($I4_1/amd$) structural transition at 1443 K [26] due to the Jahn-Teller effect at Mn_B sites. Strong lattice frustration leads to a rich magnetostructural phase diagram at low temperatures. At $T_N = 42$ K, the material undergoes paramagnetic to ferrimagnetic transition [27], adopting a triangular Yafet-Kittel [28] ferrimagnetic (YK-FiM) state [29–31]. In the YK-FiM structure, Mn_A spins are ferromagnetically aligned along $\boldsymbol{b}$, and Mn_B spins are along $-\boldsymbol{b}$ canted toward the $\pm\boldsymbol{c}$ direction [32,33]. Only a few optical measurements have been performed, reporting band gaps of 1.91 eV for bulk polycrystalline [34], 2.51 eV for thin film [35], and 2.07 eV for nanoparticles [36]. The electronic structure of the bulk Mn_3O_4 spinel has not been studied as extensively as MnO. Computational methods including Hartree-Fock [37], GGA+U, and hybrid functionals [21,34] have been employed to simulate the electronic structure using only idealized collinear magnetic structures.

α-Mn_2O_3 has multiple technological applications, such as synthesis substrate for manganite oxide perovskite compounds, starting material for lithium ion battery cathode material $LiMnO_2$ [38], and also an environmentally friendly catalyst for water purification [39] and combustion [40]. The material exists in a bixbyite structure with Mn^{3+} oxidation state [Fig. 1(c)]. For O chains along $\boldsymbol{a}$ or $\boldsymbol{b}$, there is one O atom missing per four sites, such that each O atom forms a tetrahedral linkage to surrounding Mn atoms. It undergoes cubic ($Ia3$) to orthorhombic ($Pcab$) structural transition at $T = 308$ K [41] due to the Jahn-Teller effect at Mn^{3+} sites, causing 0.8% distortion from the cubic structure. The paramagnetic to noncollinear-antiferromagnetic (NC-AFM) transition occurs at $T_{N1} = 80$–90 K and another AFM

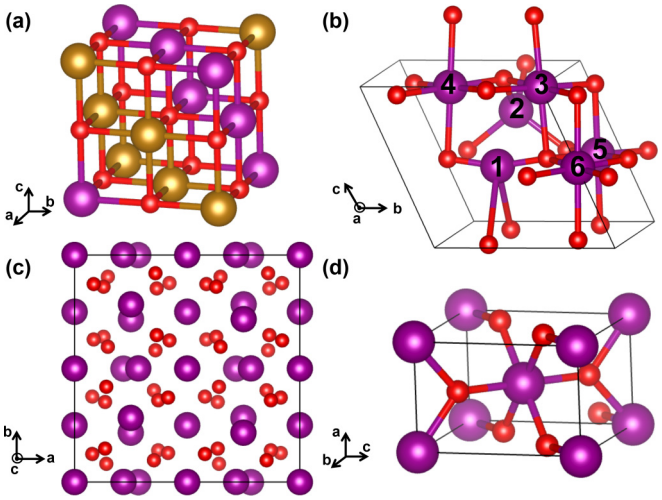

FIG. 1. Optimized crystal structures of the manganese oxides in their magnetic ground states: (a) AFM-II MnO, (b) YK-FiM Mn_3O_4, (c) NC-AFM2 α-Mn_2O_3, and (d) spiral β-MnO_2. Spin-up and spin-down Mn are colored in purple and gold for MnO, respectively, with red O atoms. The magnetic ground states of Mn_3O_4, α-Mn_2O_3, and β-MnO_2 are noncollinear; these spin structures are further discussed and illustrated in the Results and Discussion section. Bonds are not shown in (c) for clearer observation of the O chains along $\boldsymbol{a}$ or $\boldsymbol{b}$.

transition at $T_{N2} = 25$ K [42–46]. NC magnetic configuration was first proposed assuming the cubic structure [45] but was later found to be incompatible with neutron powder diffraction data [47]. An alternative collinear AFM structure with four magnetic sublattices was proposed by Regulski *et al.* [47] using the cubic lattice (indicated as AFM1 in this study). However, Cockayne *et al.* [48] found that magnetic sublattice III of the AFM1 structure is incompatible with the *Pcab* space group, and thereby proposed another collinear AFM structure using the orthorhombic lattice (indicated as AFM2 in this study), determined independently from both neutron powder diffraction and DFT+U study. Spin canting of 12°–34° was found to further improve the fitting of their diffraction data. Only one study reported the optical band gap of 1.2 eV for nanostructures [49]. The electronic structure of the bulk material has not been investigated extensively, other than two GGA+U studies [21,48] reporting different results for the magnetic ground state.

β-MnO_2 is widely used in Li-ion batteries [3,50–60], Li-O_2 batteries [61,62], supercapacitors [63–68], adsorbents [69], and catalysts [70,71]. β-MnO_2 exists in a tetragonal ($P4_2/mnm$) rutile structure with Mn^{4+} oxidation state [Fig. 1(d)]. It undergoes paramagnetic to screw-type spiral magnetic transition at $T_N = 92$ K [72], where the spins lie on the ab plane and rotate by 129° in the next adjacent layer along the c axis for a period of 7 unit cells. Transport measurements suggested a very small band gap at low temperatures [72], with one study reporting a value of 0.26 eV for epitaxially grown thin films [73]. Computational studies of the bulk material based on idealized MnF_2-type collinear AFM structure were performed using Hartree-Fock [74], GGA+U [21,75,76], and hybrid functionals [21,76]. The spiral noncollinear magnetic structure [77] has only been simulated using a tight-binding method [78] and dynamical mean-field theory [73].

These manganese oxides exhibit complex magnetic and electronic properties, making them a challenging set to study. Extensive reports on these systems have shown that rigorous theoretical methods are required to describe their properties adequately [21]. Due to the exchange-correlation functional limitations, advanced methods are needed to correctly describe the electronic structure of these strongly correlated magnetic materials. The strong electronic correlation experienced by the localized d electrons leads to unphysical self-interaction of an electron with the potential it generates. Self-interaction artificially raises the energy of the on-site single-particle energies in the Kohn-Sham equations, thereby delocalizing the localized electronic states and leading to inaccuracies in the electronic band structure. The theoretical methods developed to overcome these inherent limitations include DFT + U_{eff} [79], DFT+U+J [80–82], and hybrid functionals [83]. In DFT + U_{eff}, where $U_{\text{eff}} = U - J$, an isotropic screened on-site Coulomb interaction is added:

$$E_{\text{Hub}} = \sum_{I,\sigma} \frac{U^I_{\text{eff}}}{2} \text{Tr}[\boldsymbol{n}^{I\sigma}(\mathbf{1} - \boldsymbol{n}^{I\sigma})]. \quad (1)$$

Here, E_{Hub} is the Hubbard correction to the standard approximate DFT energy functional, I is the atomic site index, σ is the spin index, and $\boldsymbol{n}$ is the occupation matrix. In contrast, Hubbard U and J are defined distinctly in DFT+U+J, leading to a fully anisotropic treatment of the Coulomb and exchange matrices accounting for the full orbital dependence:

$$E_{\text{Hub}} = \sum_{I,\sigma} \frac{U^I - J^I}{2} \text{Tr}[\boldsymbol{n}^{I\sigma}(\mathbf{1} - \boldsymbol{n}^{I\sigma})] + \sum_{I,\sigma} \frac{J^I}{2} (\text{Tr}[\boldsymbol{n}^{I\sigma}\boldsymbol{n}^{I-\sigma}] - 2\delta_{\sigma\sigma_{\min}} \text{Tr}[\boldsymbol{n}^{I\sigma}]), \quad (2)$$

where $\sigma_{\min}$ denotes the minority spin. Compared with Eq. (1), the extra positive J term in Eq. (2) discourages interactions between electrons of antialigned spins on the same site, thereby encouraging magnetic ordering [82]. This fully anisotropic method has proven to describe strongly correlated magnetic systems more accurately [76,84]. The appropriate U value can enhance or even open up a band gap, and J can determine the noncollinear magnetic ground state, thus refining the electronic structure profile of the system. Additionally, hybrid functionals have been shown to overcome the deficiencies in describing these materials (at higher computational cost) by incorporating a fraction of the exact Hartree-Fock exchange into the exchange-correlation functional. Despite the improvements in results obtained from hybrid functionals, the DFT+U+J approach is nonetheless a computationally much cheaper alternative that is desirable in electronic structure studies involving large-scale systems, such as surfaces, supercells, interfaces, and defects.

In this work, we investigate the noncollinear magnetic ground states and the corresponding electronic structures of MnO, Mn_3O_4, α-Mn_2O_3, and β-MnO_2 using the DFT+U+J method. We show that the ground-state lattice, magnetism, and electronic structure profile can be obtained with accuracy nearing that of literature hybrid functional calculations, through careful pseudopotential design and selection of fully anisotropic U and J values.

II. METHOD AND COMPUTATIONAL DETAILS

The magnetic and electronic structures of the manganese oxides are calculated with first-principles DFT using the PBEsol [85] parametrization of the generalized gradient approximation with on-site Coloumb repulsion and exchange parameters U and J, treated separately and explicitly defined within the rotationally invariant, fully anisotropic scheme (DFT+U+J) [81,82], using the atomic orbital projection scheme [86] as implemented in the QUANTUM ESPRESSO [87] package. It has been demonstrated that the fully anisotropic J parameter plays an important role in describing strongly correlated noncollinear antiferromagnetic systems [76]. We determine the optimal Hubbard U and J values by first testing a range of values reported in the literature and changing the values as necessary, each time observing the effect on the ground-state magnetic and electronic structures and properties. We also employed the linear response method by Cococcioni *et al.* [88] to determine a range of U values; however, the values obtained by this method were too high (>7 eV) for accurate electronic structure profiles. The calculations account for spin-polarized electronic densities by treating the Mn magnetic moments as noncollinear for all systems. All atoms are represented by norm-conserving, optimized [89], designed nonlocal [90] pseudopotentials generated with the OPIUM package [91], treating the $2s$ and $2p$ of O and $3s$, $3p$, $3d$, $4s$, and $4p$ of Mn as valence states. In addition to the treatment of semicore states as valence by this Mn pseudopotential, nonlinear core-valence interaction via the partial core correction scheme [92–94] is incorporated to account for the non-negligible overlap between the core and the valence states. All calculations are run with a 70 Ry plane-wave energy cutoff to ensure accuracy for small relative energies among different magnetic configurations. The Brillouin zone is sampled using Monkhorst-Pack [95] k-point meshes of dimensions $6 \times 6 \times 6$, $8 \times 8 \times 8$, $4 \times 4 \times 4$, and $6 \times 6 \times 6$ for MnO, Mn_3O_4, α-Mn_2O_3, and β-MnO_2, respectively. A $12 \times 12 \times 12$ k-point grid is used for post-processing the electronic structure calculations for all four systems. All relaxations starting from the experimental crystal structures are performed without U and J, as relaxation with U leads to overestimated lattices and bond lengths [21]. The magnetic and electronic structures of the optimized crystal structures are then refined with U and J.

III. RESULTS AND DISCUSSION

Throughout this section, our results on the ground-state structural, magnetic, and electronic properties of the four manganese oxide systems are discussed in detail with respect to the computational parameters employed and in comparison with previously published data. Table I provides an overview of the results for each manganese oxide system from both experimental and computational studies, including DFT+U($+J$) and hybrid functional studies from the literature, in comparison to our PBEsol+U+J study.

A. MnO

Crystal structure relaxations with various imposed magnetic orders, antiferromagnetic (AFM-II, A-AFM, C-AFM) and ferromagnetic (FM), reveal the AFM-II structure as the magnetic ground state (Table II). The lattice constant, a = 4.40 Å, is 0.68% smaller than the literature value of 4.43 Å [96]. PBEsol therefore yields structural properties that are in good agreement with the experimental values. Other AFM orders result in $c < a$, inconsistent with experimental data, while FM order produces a severely contracted lattice structure.

Electronic structure calculation without U and J shows an underestimated band gap of 1.16 eV, consistent with previous GGA studies [15–18,20,23]. Applying $U = 4$ eV increases the band gap to 3.32 eV; this value is higher compared to other DFT + U_{eff}. For example, Franchini *et al.* [16] obtained a band gap of 2.03 eV with $U = 6$ eV; they were able to increase the band gap to 3 eV only by increasing the U value up to 15 eV. Since our calculation requires much lower U value to achieve a more reasonable band gap, it suggests enhanced performance of our designed pseudopotential.

Despite moving the band gap closer to the experimental value, the electronic structure profile is compromised by U when compared with those reported by hybrid functional calculations [15–17,21,25], as U shifts the energies of the valence and conduction bands further apart. Previous GW studies reported that large values of U reorder the bands when compared to the GW quasiparticle band structures [24,101]. We find that applying an anisotropic $J = 1.2$ eV enhances the profile significantly, but it reduces the band gap to 2.81 eV [Fig. 2(a)]. Explicitly defined Hubbard J takes into account the full symmetry of d-d interactions, thereby providing a better description of orbital spin polarizations [76]. In our orbital-projected density of states (DOS), the highest-energy valence band shows strong mixing of O $2p$ and Mn e_g states enhanced by U, whereas the lowest-energy conduction band primarily consists of Mn t_{2g} states. Together with the calculated magnetic moment of 4.56 μ_B, in good agreement with the experimental value of 4.58 μ_B [97], our electronic structure predicts MnO as a high-spin insulator of intermediate Mott-Hubbard/charge-transfer character, consistent with results from previous high-level computational studies [12,15–17,25].

B. Mn_3O_4

We determine the ground-state magnetic structure of Mn_3O_4 to be the experimentally reported YK-FiM structure. This noncollinear structure is 152 meV lower in energy than the lowest collinear structure. The YK-FiM structure has not been computed before; therefore, we start by comparing our results with previous calculations on idealized collinear structures. We compute the six idealized collinear FiM configurations (FiM1–6), in addition to the FM order, as first specified in the Hartree-Fock study of Chartier *et al.* [37]. Six Mn atoms of the unit cell are numbered as shown in Fig. 1(b), where two Mn_A are Mn1–2, two Mn_B along $\boldsymbol{b}$ are Mn3–4, and two Mn_B along $\boldsymbol{a}$ are Mn5–6. Crystal structure relaxation with the six imposed FiM orders shows FiM6 (↑↓↑↓↑↓) as the lowest-energy structure when the spins are held collinear. In FiM6 order, all spins are antiferromagnetic to all their neighbors, which is consistent with the experimental measurements reporting the exchange interaction constants to be antiferromagnetic [31,102,103]. However, the net magnetic moment is zero in FiM6, which is inconsistent with the experimentally observed net magnetic

TABLE I. Ground-state magnetism, lattice, magnetic moment per Mn, and band gap for each manganese oxide system reported by (1) experimental studies, (2) literature DFT+U(+J), and (3) literature hybrid functional studies, in direct comparison to (4) our PBEsol+U+J results. Our lattice constants presented here are values optimized without U and J.

System	Method	Magnetic state	Lattice constants (Å)	Magnetic moment (μ_B)	E_g (eV)
MnO	(1) Experimental	AFM-II	$a = 4.43$ [96]	4.58 [97]	3.6–4.2 [10,11]
	(2) PBE+U, $U = 4$ eV [23]	AFM-II	$a = 4.489$	4.60	2.34
	(3) PBE0 [16]	AFM-II	$a = 4.40$	4.52	4.02
	(4) PBEsol+U+J, $U = 4$ eV, $J = 1.2$ eV	AFM-II	$a = 4.40$	4.56	2.81
Mn_3O_4	(1) Experimental	YK-FiM	$a = 5.71$, $c = 9.35$ [33] $V_0 = 155.73$ Å^3 [98]	4.34, 3.64, 3.25 [33]	1.91 [34]
	(2) PBE+U, $U = 5$ eV [34]	FiM6	N/A	4.6, 3.9	1.46
	(3) PBE0 [21]	FiM3	$V_0 = 157.42$ Å^3	3.69–4.50	2.4
	(4) PBEsol+U+J, $U = 4$ eV, $J = 1.2$ eV	YK-FiM	$a = 5.76$, $c = 9.35$ $V_0 = 155.50$ Å^3	4.49, 3.74, 3.69	1.01
α-Mn_2O_3	(1) Experimental	NC-AFM2 [48]	$a = 9.407$, $b = 9.447$, $c = 9.366$, $V_0 = 834.48$ Å^3 [41]	3.3–4.0 [47] 2.6–3.5 [48]	1.2 [49]
	(2) PBEsol+U+J, $U = 2.8$ eV, $J = 1.2$ eV [48]	AFM2	$a = 9.402$, $b = 9.444$, $c = 9.367$	3.6	0.6
	(3) HSE [21]	FM	$V_0 = 845.83$ Å^3	3.81–3.84	0.1
	(4) PBEsol+U+J, $U = 2.8$ eV, $J = 1.2$ eV	NC-AFM2	$a = 9.382$, $b = 9.444$, $c = 9.376$, $V_0 = 830.71$ Å^3	4.09, 2.91, 3.68, 3.83, 3.69	0.081
β-MnO_2	(1) Experimental	Spiral	$a = 4.396$, $c = 2.871$ $V_0 = 55.48$ Å^3 [99]	2.35 [100]	0.26 [73]
	(2) GGA+U+J, $U = 6.7$ eV, $J = 1.2$ eV [76]	AFM	$a = 4.45$, $c = 2.936$	2.96	0.8
	(3) PBE0 [21]	AFM	$V_0 = 55.06$ Å^3	2.89	1.5
	(4) PBEsol+U+J, $U = 2.8$ eV, $J = 1.2$ eV	Spiral	$a = 4.402$, $c = 2.880$ $V_0 = 55.80$ Å^3	2.63	0.25

moment of 1.84 μ_B per formula unit along $\boldsymbol{b}$ [30,32,33,104]. The idealized collinear FiM configuration most consistent with the experimentally observed YK-FiM structure would be FiM4 (↑↑↑↓↑↓), where Mn_A spins (Mn1–2) are ferromagnetically aligned, and all Mn_B spins (Mn3–6) are antiferromagnetically aligned. We find that applying $U = 4$ eV and $J = 1.2$ eV to the relaxed structures lowers the energy of the FiM4 structure, making it the lowest-energy collinear magnetic state (Table III). However, once the spins are allowed to be noncollinear, the YK-FiM structure is the most energetically favorable. The lattice constants obtained with FiM4 order are $a = 5.76$ Å and $c = 9.35$ Å, in good agreement with the experimental values of $a = 5.71$ Å and $c = 9.35$ Å reported by neutron diffraction study of a single-crystal sample [33].

TABLE II. Relaxed lattice constants and relative energies per formula unit of MnO with various imposed magnetic orders. Experimental lattice constant is $a = 4.43$ Å [96] with the AFM-II ground state.

Magnetism	Lattice constants (Å)	Relative E (meV/f.u.)
AFM-II	$a = 4.40$	0
C-AFM	$a = 4.41$, $c = 4.38$	17
A-AFM	$a = 4.43$, $c = 4.38$	80
FM	$a = 4.29$	413

In contrast to our results, previous computational studies reported FiM3 (↑↑↓↓↑↑) [21] and FiM6 (↑↓↑↓↑↓) [34,37] as the magnetic ground state. FiM3 order describes intrachain B-B interactions to be ferromagnetic, which is inconsistent with the experimental observations of the interaction to be strongly antiferromagnetic [31,102,103,105]. To justify FiM4 (↑↑↑↓↑↓) as the idealized collinear magnetic ground state, we calculated four exchange interaction constants: J_{AA}, J_{AB}, $J_{BB\mathrm{sr}}$, and $J_{BB\mathrm{lr}}$, where the last two values represent intrachain (short-range) and interchain (long-range) B-B interactions, respectively. We map the energies of the six FiM structures, relative to that of the FM structure, to a Heisenberg Hamiltonian, as described in Ref. [37]. All interactions are antiferromagnetic, with small values involving the tetrahedral Mn_A site ($J_{AA} = -0.36$ K and $J_{AB} = -2.98$ K), large and dominant intrachain B-B interaction ($J_{BB\mathrm{sr}} = -23.9$ K), and small interchain B-B interaction ($J_{BB\mathrm{lr}} = -0.45$ K). The J values are in reasonable agreement with the experimental values obtained from a polycrystalline sample [31] ($J_{AA} = -4.9$ K, $J_{AB} = -6.8$ K, and $J_{BB} = -19.9$ K). The strong

TABLE III. Relaxed lattice constants of Mn_3O_4 with various imposed magnetic orders, in addition to relative energies per formula unit and magnetic moments per Mn obtained with $U = 4$ eV and $J = 1.2$ eV. Experimental lattice constants are $a = 5.71$ Å and $c = 9.35$ Å, and the experimental magnetic moments are 4.34, 3.64, and 3.25 μ_B for tetrahedral Mn, octahedral Mn along b, and octahedral Mn along a, respectively [33] with the YK-FiM ground state.

Magnetism	Lattice constants (Å)	Relative E (meV/f.u.)	Magnetic moment (μ_B)
YK-FiM	$a = 5.76, c = 9.35$	0	4.49, 3.74, 3.69
FiM4 (↑↑↑↓↑↓)	$a = 5.76, c = 9.35$	152	4.50, 3.85, 3.65
FiM1 (↓↓↑↑↑↑)	$a = 5.74, c = 9.37$	154	4.48, 3.67
FiM6 (↑↓↑↓↑↓)	$a = 5.76, b = 5.78, c = 9.32$	158	4.48, 3.76
FiM3 (↑↑↓↓↑↑)	$a = 5.75, c = 9.34$	175	4.50, 3.85, 3.65
FiM2 (↑↓↑↑↑↑)	$a = 5.77, c = 9.35$	184	4.51, 3.78
FiM5 (↑↑↑↓↑↑)	$a = 5.81, b = 5.78, c = 9.36$	193	4.50, 3.86, 3.66
FM (↑↑↑↑↑↑)	$a = 5.82, c = 9.36$	208	4.52, 3.87

antiferromagnetic intrachain B-B interaction can be understood as a result of the direct exchange between overlapping neighboring Mn_B t_{2g} orbitals (J_{BBsr}) dominating over very weak ferromagnetic superexchange mediated by O $2p$ orbitals (J_{BBlr}) [103].

The noncollinear magnetic ground state shows an exotic spin pattern, illustrated in Fig. 3. All the spins lie on the bc plane. Mn_A spins are aligned along the b axis, as if they were ferromagnetic in that direction, with small deviations from the b axis. However, Mn_B spins show a sinusoidal spin pattern

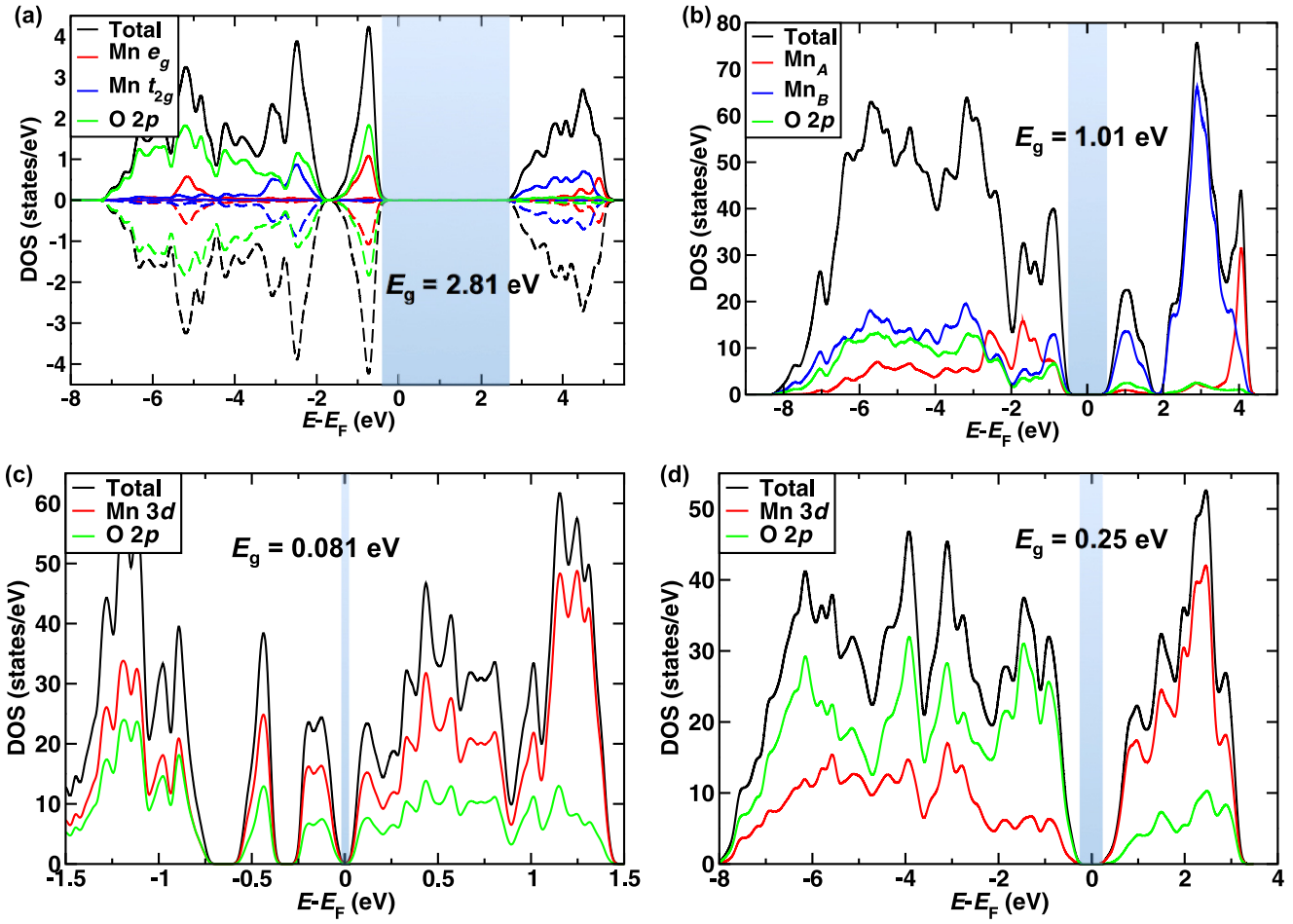

FIG. 2. Projected density of states of the manganese oxides computed with PBEsol+U+J: (a) MnO shows a collinear AFM-II ground state with a band gap of 2.81 eV; the valence bands are governed by the overlap between O $2p$ and Mn e_g orbitals, and the conduction bands by Mn t_{2g} orbitals. The rest of the systems have noncollinear magnetic ground states: (b) Mn_3O_4 shows a YK-FiM ground state with a band gap of 1.01 eV, where Mn_A and Mn_B refer to the tetrahedral and the octahedral sites, respectively; (c) α-Mn_2O_3 shows a NC-AFM2 ground state with a small band gap of 0.081 eV; (d) β-MnO_2 shows a spiral magnetic ground state with a band gap of 0.25 eV. The band gap regions are indicated with a light blue color.

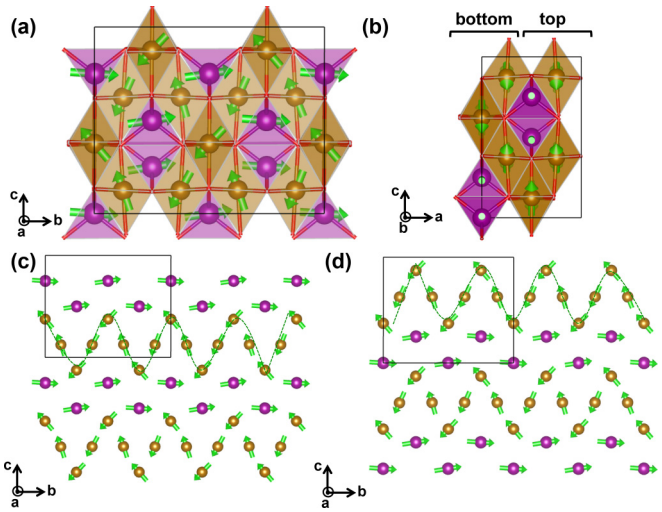

FIG. 3. Computed YK-FiM structure of Mn_3O_4: (a) Magnetic moments are colored in green within the Mn tetrahedral (purple) and octahedral (gold) cages. (b) Side view showing the top and bottom bilayers used to illustrate the noncollinear spin pattern. (c) Top bilayer exhibiting a sinusoidal Mn_B spin pattern (along the green dashed lines), with Mn_A spin alignment along the b axis. (d) The bottom bilayer shows a similar spin structure, but the pattern is related by mirror symmetry to the one shown in (c).

that is related by mirror symmetry for different bilayers of the system [Figs. 3(c) and 3(d)]. Calculating the electronic structure of the YK-FiM ground state with $U = 4$ eV and $J = 1.2$ eV yields a band gap of 1.01 eV [Fig. 2(b)]. This opening of a gap is remarkable when compared with the PBE+U study of Franchini *et al.* [21], where only half-metallic states with gaps of 0.3–0.5 eV were obtained with $U = 3$–6 eV for FiM3 order. Since our noncollinear magnetic ground state is the experimentally reported structure, YK-FiM, rather than FiM3 [21] or FiM6 [34,37], the electronic structure profile cannot be directly compared with those reported by the previous computational studies. However, several features are in agreement. The valence band consists of widely spread Mn $3d$ states with a large mixing of O $2p$ states. The conduction band mostly consists of Mn_B $3d$ states, with a characteristic splitting of ≈0.21 eV, which was also reported by Hirai *et al.* [34] as well. The calculated magnetic moments are 4.49, 3.74, and 3.69 μ_B for the spins of Mn_A, Mn_B along b, and Mn_B along a, respectively, in good agreement with the experimental values of 4.34, 3.64, and 3.25 μ_B reported by neutron diffraction study of a single-crystal sample [33]. The splitting of the Mn_B magnetic moment was also observed by a ^{55}Mn NMR study [106]. Our study predicts Mn_3O_4 as an insulator with the YK-FiM ground state, in agreement with the experimental reports.

C. α-Mn_2O_3

We compute the magnetic and electronic structures of α-Mn_2O_3 using the AFM orderings proposed by Regulski *et al.* [47] (AFM1) and Cockayne *et al.* [48] (AFM2) while allowing spin noncollinearity. Cockayne *et al.* [48] determined the NC-AFM2 order to be the magnetic ground state [Figs. 4(a) and 4(b)], independently from neutron powder diffraction and PBEsol+U+J study in concurrence with a cluster-expansion model, suggesting that the ground-state magnetic structure of α-Mn_2O_3 has largely been solved. In agreement with this observation, our structural, electronic, and magnetic relaxations with each candidate magnetic order confirm the NC-AFM2 structure as the magnetic ground state [Fig. 4(a)]. Applying $U = 2.8$ eV and $J = 1.2$ eV further stabilizes the NC-AFM2 structure (Table IV). This complex spin structure is easier to understand in terms of four magnetic sublattices [Figs. 4(c) and 4(d)]. These four magnetic sublattices correspond to the Mn Wyckoff positions: sublattice I consists of Mn 4(a) and Mn 4(b), and sublattices II–IV consist of Mn 8(c) with different spin patterns. The spin deviation from the c axis varies from 4°–23°, as shown in Table V, in general agreement with the experimental work, where the spins deviate in a range of 12°−34°. More importantly, our computed electronic structure shows a band gap of 0.081 eV [Fig. 4(b)]. Although our results are consistent with the experimental and theoretical work presented by Cockayne *et al.* [48], they are in disagreement with the results reported by Franchini *et al.* [21], where both PBE+U and hybrid functional calculations, HSE and PBE0, yielded the FM ground state. This disagreement suggests that those levels of theory incorrectly predict the ground state of this complex magnetic system and that a noncollinear description of this system is needed. As for the lattice structure, relaxation with the AFM2 order yields $a = 9.382$ Å, $b = 9.444$ Å, and $c = 9.376$ Å, in good agreement with the experimental values of $a = 9.408$ Å, $b = 9.449$ Å, and $c = 9.374$ Å [48].

Calculating the electronic structure of the NC-AFM2 order with $U = 2.8$ eV and $J = 1.2$ eV yields an insulating state with a gap of 0.081 eV [Fig. 2(c)], with the projected DOS profile in good agreement with that reported by Cockayne *et al.* [48]. The calculated magnetic moments, shown in Table V, are in general agreement with the experimental values of Cockayne *et al.* [48], which vary from 2.6–4.0 μ_B. Within the framework of DFT+U+J, our study predicts α-Mn_2O_3 as an insulator with the NC-AFM2 ground state, in agreement with the experimental observations. Achieving accurate magnetic properties with our computational setup is a significant leap forward to understanding these complex magnetic systems.

D. β-MnO_2

To compute the magnetic structure of β-MnO_2, we use the screw-type spiral order, in addition to the AFM and FM orders that previous computational studies have employed [21,74–76]. Crystal and magnetic structure relaxations yield the spiral structure as the magnetic ground state (Table VI). The lattice constants, $a = 4.402$ Å and $c = 2.880$ Å, are in excellent agreement with the experimental values of $a = 4.404$ Å and $c = 2.877$ Å [108,109]. The spiral structure (Fig. 5) consists of spins on the ab plane rotating by 129° across each layer along the c axis. A total of seven unit cells (14 layers) are needed for a complete magnetic spiral period (5 spin revolutions).

Calculating the electronic structure of the spiral order with $U = 2.8$ eV and $J = 1.2$ eV yields an insulating state with a gap of 0.25 eV [Fig. 2(d)], in good agreement with the value of

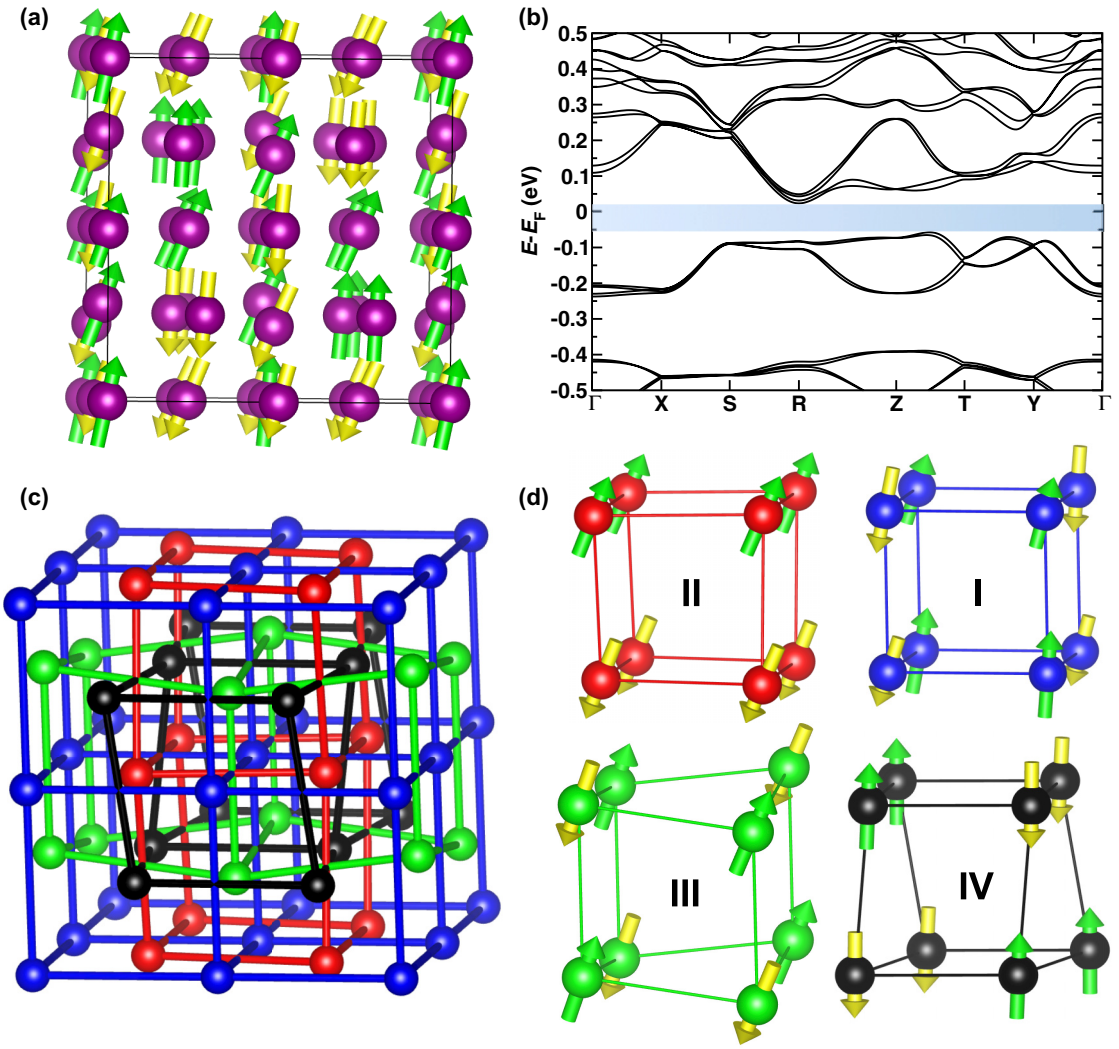

FIG. 4. Magnetic and electronic structures of α-Mn_2O_3: (a) Computed NC-AFM2 structure, with green and yellow spins indicating up and down directions, respectively. (b) The corresponding band structure shows an insulating state with a gap of 0.081 eV. (c) Four magnetic sublattices based on Mn Wyckoff positions. (d) The magnetic sublattices from (c) untangled for clarity, where sublattice I consists of Mn 4(a) and 4(b) in a C-type magnetic structure, sublattice II consists of Mn 8(c) in an A-type magnetic structure, sublattice III consists of Mn 8(c) in a G-type magnetic structure, and sublattice IV consists of Mn 8(c) in a unique magnetic structure, where each magnetic ion has three nearest neighbors, one with identical spin direction and two with opposite spin direction, similar to E type [107].

0.27 eV reported by the PBEsol+U+J study [75] and 0.26 eV reported by optical measurements of a thin-film sample [73]. Similar to Mn_3O_4, the opening of a gap is remarkable when compared with PBE+U study of Franchini *et al.* [21], where only metallic states were obtained with U values up to 6 eV. The projected DOS profile is also in excellent agreement with that reported by hybrid functional calculations of Franchini *et al.* [21]. In accordance with the Mn^{4+} oxidation state and the octahedral crystal-field splitting, the valence band shows a

TABLE IV. Relaxed lattice constants of α-Mn_2O_3 with various imposed magnetic orders, in addition to relative energies per formula unit obtained with $U = 2.8$ eV and $J = 1.2$ eV. Experimental lattice constants are $a = 9.407$ Å, $b = 9.447$ Å, and $c = 9.366$ Å [41] with the NC-AFM2 ground state [48].

Magnetism	Lattice constants (Å)	Relative E (meV/f.u.)
NC-AFM2	$a = 9.382$, $b = 9.444$, $c = 9.376$	0
NC-AFM1	$a = 9.410$, $b = 9.387$, $c = 9.399$	4.1
FM	$a = 9.438$	50

TABLE V. Magnetic moments per Mn and spin angles for the NC-AFM2 structure of α-Mn_2O_3, based on the five unique Mn Wyckoff positions. The spin angles are relative to the c axis. The experimental magnetic moments are in the range of 2.6–4.0 μ_B [47,48].

Mn Wyckoff position	Magnetic moment (μ_B)	Spin angle (°)
Mn 4(a)	4.09	8.7
Mn 4(b)	2.91	17.3
Mn 8(c)	3.68	23.4
Mn 8(c)	3.83	21.8
Mn 8(c)	3.69	4.5

TABLE VI. Relaxed lattice constants of β-MnO_2 with different imposed magnetic orders, in addition to relative energies per formula unit and magnetic moments per Mn obtained with $U = 2.8$ eV and $J = 1.2$ eV. Experimental lattice constants are $a = 4.396$ Å and $c = 2.871$ Å [99], and the magnetic moment is 2.35 μ_B [100] with the spiral magnetic ground state.

Magnetism	Lattice constants (Å)	Relative E (meV/f.u.)	Magnetic moment (μ_B)
Spiral	$a = 4.402, c = 2.88$	0	2.63
AFM	$a = 4.402, c = 2.88$	47	2.65
FM	$a = 4.422, c = 2.89$	650	2.91

single broad Mn t_{2g} band with a large mixing of O $2p$ states, whereas the conduction band consists mostly of Mn e_g states with small O $2p$ mixing. The calculated magnetic moment of 2.63 μ_B is in good agreement with the experimental value of 2.35 μ_B reported by neutron powder diffraction study [100]. Our electronic structure accurately predicts β-MnO_2 as an insulator with the spiral magnetic ground state.

IV. SUMMARY AND CONCLUSIONS

Our computational study of manganese oxides, using the fully anisotropic PBEsol+U+J approach, yields ground-state structural, magnetic, and electronic properties of quality and accuracy that are comparable to previously reported hybrid functional and experimental studies. We show that the limitations of conventional DFT regarding the magnetic and electronic structures of insulating transition metal oxides can be improved by pseudopotential design and careful selection of fully anisotropic U and J values. The resulting magnetic ground states (AFM-II, YK-FiM, NC-AFM2, and spiral for MnO, Mn_3O_4, α-Mn_2O_3, and β-MnO_2, respectively) correspond to the experimentally observed configurations. All relaxed lattice constants, obtained with PBEsol alone, are in good agreement with the experimental values. Appropriate band gaps were obtained with U values smaller than those used by previous GGA+U studies, while reproducing the electronic structure profiles in good agreement with those reported by previous hybrid functional studies. Our results overall suggest the enhanced performance of our designed pseudopotential with semicore and partial core correction, thereby offering a promising potential of the DFT+U+J approach for electronic structure studies involving other strongly correlated, complex magnetic systems with accuracy nearing that of more computationally expensive methods such as hybrid functionals.

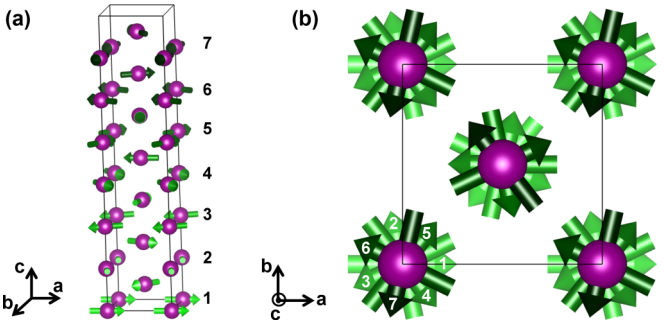

FIG. 5. Computed spiral magnetic structure of β-MnO_2: (a) Side view showing the seven unit cell period of the spin spiral, numbered for clarity, with magnetic moments colored in green. (b) Top view showing the spin rotation of 129° from each layer. The darker the spin, the closer it is to the viewer.

ACKNOWLEDGMENTS

The authors acknowledge support from the Department of Energy, Division of Basic Energy Sciences, under Grant No. DE-FG02-07ER15920. J.S.L. wishes to thank the Vagelos Integrated Program in Energy Research (VIPER) at the University of Pennsylvania. Computational support was provided by the High-Performance Computing Modernization Office and the National Energy Research Scientific Computing Center.

[1] Z. Yang, Y. Zhang, W. Zhang, X. Wang, Y. Qian, X. Wen, and S. Yang, J. Solid State Chem. **179**, 679 (2006).
[2] M. M. Thackeray, W. I. F. David, P. G. Bruce, and J. B. Goodenough, Mater. Res. Bull. **18**, 461 (1983).
[3] M. M. Thackeray, Prog. Solid State Chem. **25**, 1 (1997).
[4] G. H. Lee, S. H. Huh, J. W. Jeong, B. J. Choi, S. H. Kim, and H.-C. Ri, J. Am. Chem. Soc. **124**, 12094 (2002).
[5] S. Thota, B. Prasad, and J. Kumar, Mater. Sci. Eng. B **167**, 153 (2010).
[6] R. Jothiramalingam and M. K. Wang, J. Porous Mater. **17**, 677 (2010).
[7] C. Kittel, *Introduction to Solid State Physics* (Wiley, New York, 1986).
[8] G. A. Slack, J. Appl. Phys. **31**, 1571 (1960).
[9] H. Shaked, J. Faber Jr., and R. L. Hitterman, Phys. Rev. B **38**, 11901 (1988).
[10] R. N. Iskenderov, I. A. Drabkin, L. T. Emel'yanova, and Y. M. Ksendzov, Sov. Phys. Solid State **10**, 2031 (1969).
[11] J. van Elp, R. H. Potze, H. Eskes, R. Berger, and G. A. Sawatzky, Phys. Rev. B **44**, 1530 (1991).
[12] W. C. Mackrodt, N. M. Harrison, V. R. Saunders, N. L. Allan, M. D. Towler, E. Apra, and R. Dovesi, Philos. Mag. A **68**, 653 (1993).
[13] M. D. Towler, N. L. Allan, N. M. Harrison, V. R. Saunders, W. C. Mackrodt, and E. Apra, Phys. Rev. B **50**, 5041 (1994).
[14] S. Massidda, M. Posternak, A. Baldereschi, and R. Resta, Phys. Rev. Lett. **82**, 430 (1999).
[15] X. Feng, Phys. Rev. B **69**, 155107 (2004).
[16] C. Franchini, V. Bayer, R. Podloucky, J. Paier, and G. Kresse, Phys. Rev. B **72**, 045132 (2005).
[17] A. Schrön, C. Rödl, and F. Bechstedt, Phys. Rev. B **82**, 165109 (2010).
[18] P. Dufek, P. Blaha, V. Sliwko, and K. Schwarz, Phys. Rev. B **49**, 10170 (1994).
[19] J. Hugel and M. Kamal, Solid State Commun. **100**, 457 (1996).

[20] J. E. Pask, D. J. Singh, I. I. Mazin, C. S. Hellberg, and J. Kortus, Phys. Rev. B **64**, 024403 (2001).
[21] C. Franchini, R. Podloucky, J. Paier, M. Marsman, and G. Kresse, Phys. Rev. B **75**, 195128 (2007).
[22] A. Schron, C. Rodl, and F. Bechstedt, Phys. Rev. B **86**, 115134 (2012).
[23] A. Schron, M. Granovskij, and F. Bechstedt, J. Phys.: Condens. Matter **25**, 094006 (2013).
[24] H. Jiang, R. I. Gomez-Abal, P. Rinke, and M. Scheffler, Phys. Rev. B **82**, 045108 (2010).
[25] E. Engel and R. N. Schmid, Phys. Rev. Lett. **103**, 036404 (2009).
[26] J. B. Goodenough and A. L. Loeb, Phys. Rev. **98**, 391 (1955).
[27] A. S. Borovik-Romanov and M. P. Orlova, J. Exptl. Theoret. Phys. **32**, 1255 (1957).
[28] Y. Yafet and C. Kittel, Phys. Rev. **87**, 290 (1952).
[29] I. S. Jacobs, J. Phys. Chem. Solids **11**, 1 (1959).
[30] K. Dwight and N. Menyuk, Phys. Rev. **119**, 1470 (1960).
[31] G. Srinivasan and M. S. Seehra, Phys. Rev. B **28**, 1 (1983).
[32] B. Boucher, R. Buhl, and M. Perrin, J. Appl. Phys. **42**, 1615 (1971).
[33] G. B. Jensen and O. V. Nielsen, J. Phys. C: Solid State Phys. **7**, 409 (1974).
[34] S. Hirai, Y. Goto, A. Wakatsuki, Y. Kamihara, M. Matoba, and W. L. Mao, arXiv:1406.4486v1.
[35] D. P. Dubal, D. S. Dhawale, R. R. Salunkhe, V. J. Fularim, and C. D. Lokhande, J. Alloys Compd. **497**, 166 (2010).
[36] A. Jha, R. Thapa, and K. K. Chattopadhyay, Mater. Res. Bull. **47**, 813 (2012).
[37] A. Chartier, P. D'Arco, R. Dovesi, and V. R. Saunders, Phys. Rev. B **60**, 14042 (1999).
[38] Q. Liu, Y. Li, Z. Hu, D. Mao, C. Chang, and F. Huang, Electrochim. Acta **53**, 7298 (2008).
[39] N. N. Tusar, D. Maucec, M. Rangus, I. Arcon, M. Mozaj, M. Cotman, A. Pintar, and V. Kaucic, Adv. Funct. Mater. **22**, 820 (2012).
[40] M. Baldi, V. S. Escribano, J. M. G. Amores, F. Milella, and G. Busca, Appl. Catal. B: Environ. **17**, L175 (1998).
[41] S. Geller, Acta Cryst. **27**, 821 (1970).
[42] E. G. King, J. Am. Chem. Soc. **76**, 3289 (1954).
[43] J. Cable, M. Wilkinson, E. Woolan, and W. Koehler, Phys. Prog. Rep. **43**, 2302 (1957).
[44] R. R. Chevalier, G. Roult, and E. F. Bertaut, Solid State Commun. **5**, 7 (1967).
[45] R. W. Grant, S. Geller, J. A. Cape, and G. P. Espinosa, Phys. Rev. **175**, 686 (1968).
[46] S. Geller and G. P. Espinosa, Phys. Rev. B **1**, 3763 (1970).
[47] M. Regulski, R. Przenioslo, I. Sosnowska, D. Hohlwein, and R. Schneider, J. Alloys Compd. **362**, 236 (2004).
[48] E. Cockayne, I. Levin, H. Wu, and A. Llobet, Phys. Rev. B **87**, 184413 (2013).
[49] Q.-u.-a. Javed, W. Feng-Ping, M. Y. Rafique, A. M. Toufiq, and M. Z. Iqbal, Chin. Phys. B **21**, 117311 (2012).
[50] J. M. Tarascon and D. Guyomard, Electrochim. Acta **38**, 1221 (1993).
[51] G. Pistoia and G. Wang, Solid State Ionics **66**, 135 (1993).
[52] H. Huang and P. G. Bruce, J. Power Sources **54**, 52 (1995).
[53] A. R. Armstrong and P. G. Bruce, Nature (London) **381**, 499 (1996).
[54] X. Wang and Y. Li, J. Am. Chem. Soc. **124**, 2880 (2002).
[55] W. Tang, X. Yang, Z. Liu, and K. Ooi, J. Mater. Chem. **13**, 2989 (2003).
[56] F. Cheng, J. Zhao, W. Song, C. Li, H. Ma, J. Chen, and P. Shen, Inorg. Chem. **45**, 2038 (2006).
[57] J.-Y. Luo, J.-J. Zhang, and Y.-Y. Xia, Chem. Mater. **18**, 5618 (2006).
[58] F. Jiao and P. G. Bruce, Adv. Mater. **19**, 657 (2007).
[59] V. Mathew, J. Lim, J. Kang, J. Gim, A. K. Rai, and J. Kim, Electrochem. Commun. **13**, 730 (2011).
[60] D. Wang, L.-M. Liu, S.-J. Zhao, B.-H. Li, H. Liu, and X.-F. Lang, Phys. Chem. Chem. Phys. **15**, 9075 (2013).
[61] A. Debart, A. J. Paterson, J. Bao, and P. G. Bruce, Angew. Chem. Int. Ed. **47**, 4521 (2008).
[62] A. K. Thapa, Y. Hidaka, H. Hagiwara, S. Ida, and T. Ishihara, J. Electrochem. Soc. **158**, A1483 (2011).
[63] M. Toupin, T. Brousse, and D. Belanger, Chem. Mater. **14**, 3946 (2002).
[64] V. Subramanian, H. Zhu, R. Vajtai, P. M. Ajayan, and B. Wei, J. Phys. Chem. B **109**, 20207 (2005).
[65] S. Devaraj and N. Munichandraiah, J. Phys. Chem. C **112**, 4406 (2008).
[66] H. Zhang, G. Cao, Z. Wang, Y. Yang, Z. Shi, and Z. Gu, Nano Lett. **8**, 2664 (2008).
[67] X. Lang, A. Hirata, T. Fujita, and M. Chen, Nat. Nanotechnol. **6**, 232 (2011).
[68] J. Zang and X. Li, J. Mater. Chem. **21**, 10965 (2011).
[69] L. Espinal, W. Wong-Ng, J. A. Kaduk, A. J. Allen, C. R. Snyder, C. Chiu, D. W. Siderius, L. Li, E. Cockayne, A. E. Espinal, and S. L. Suib, J. Am. Chem. Soc. **134**, 7944 (2012).
[70] R. Andreozzi, A. Insola, V. Caprio, R. Marotta, and V. Tufano, Appl. Catal. A: General **138**, 75 (1996).
[71] F. H. B. Lima, M. L. Calegaro, and E. A. Ticianelli, Electrochim. Acta **52**, 3732 (2007).
[72] H. Sato, T. Enoki, M. Isobe, and Y. Ueda, Phys. Rev. B **61**, 3563 (2000).
[73] X. L. Yu, S. X. Wu, Y. J. Liu, and S. W. Li, Solid State Commun. **146**, 166 (2008).
[74] W. C. Mackrodt and E.-A. Williamson, J. Chem. Soc., Faraday Trans. **93**, 3295 (1997).
[75] E. Cockayne and L. Li, Chem. Phys. Lett. **544**, 53 (2012).
[76] D. A. Tompsett, D. S. Middlemiss, and M. S. Islam, Phys. Rev. B **86**, 205126 (2012).
[77] A. Yoshimori, J. Phys. Soc. Jpn. **14**, 807 (1959).
[78] M. Zhuang and J. W. Halley, Phys. Rev. B **64**, 024413 (2001).
[79] S. L. Dudarev, G. A. Botton, S. Y. Savrasov, C. J. Humphreys, and A. P. Sutton, Phys. Rev. B **57**, 1505 (1998).
[80] V. I. Anisimov, J. Zaanen, and O. K. Andersen, Phys. Rev. B **44**, 943 (1991).
[81] A. I. Liechtenstein, V. I. Anisimov, and J. Zaanen, Phys. Rev. B **52**, R5467 (1995).
[82] B. Himmetoglu, R. M. Wentzcovitch, and M. Cococcioni, Phys. Rev. B **84**, 115108 (2011).
[83] A. D. Becke, J. Chem. Phys. **98**, 1372 (1993).
[84] E. Bousquet and N. Spaldin, Phys. Rev. B **82**, 220402 (2010).
[85] J. P. Perdew, A. Ruzsinszky, G. I. Csonka, O. A. Vydrov, G. E. Scuseria, L. A. Constantin, X. Zhou, and K. Burke, Phys. Rev. Lett. **100**, 136406 (2008).
[86] Y.-C. Wang, Z.-H. Chen, and H. Jiang, J. Chem. Phys. **144**, 144106 (2016).

[87] P. Giannozzi, S. Baroni, N. Bonini, M. Calandra, R. Car, C. Cavazzoni, D. Ceresoli, G. L. Chiarotti, M. Cococcioni, I. Dabo, A. Dal Corso, S. de Gironcoli, S. Fabris, G. Fratesi, R. Gebauer, U. Gerstmann, C. Gougoussis, A. Kokalj, M. Lazzeri, L. Martin-Samos, N. Marzari, F. Mauri, R. Mazzarello, S. Paolini, A. Pasquarello, L. Paulatto, C. Sbraccia, S. Scandolo, G. Sclauzero, A. P. Seitsonen, A. Smogunov, P. Umari, and R. M. Wentzcovitch, J. Phys.: Condens. Matter **21**, 395502 (2009).

[88] M. Cococcioni and S. de Gironcoli, Phys. Rev. B **71**, 035105 (2005).

[89] A. M. Rappe, K. M. Rabe, E. Kaxiras, and J. D. Joannopoulos, Phys. Rev. B **41**, 1227 (1990).

[90] N. J. Ramer and A. M. Rappe, Phys. Rev. B **59**, 12471 (1999).

[91] See http://opium.sourceforge.net

[92] S. G. Louie, S. Froyen, and M. L. Cohen, Phys. Rev. B **26**, 1738 (1982).

[93] M. Fuchs and M. Scheffler, Comput. Phys. Commun. **119**, 67 (1999).

[94] D. Porezag, M. R. Pederson, and A. Y. Liu, Phys. Rev. B **60**, 14132 (1999).

[95] H. J. Monkhorst and J. D. Pack, Phys. Rev. B **13**, 5188 (1976).

[96] S. Sasaki, K. Fujino, Y. Takeuchi, and R. Sadanaga, Acta Cryst. **A36**, 904 (1980).

[97] A. K. Cheetham and D. A. O. Hope, Phys. Rev. B **27**, 6964 (1983).

[98] R. G. Wyckoff, *Crystal Structures* (Wiley, New York, 1963).

[99] N. Ohama and Y. Hamaguchi, J. Phys. Soc. Jpn. **30**, 1311 (1971).

[100] M. Regulski, R. Przenioslo, I. Sosnowska, and J.-U. Hoffmann, Phys. Rev. B **68**, 172401 (2003).

[101] C. Rodl, F. Fuchs, J. Furthmuller, and F. Bechstedt, Phys. Rev. B **79**, 235114 (2009).

[102] B. Mehdaoui, O. Pena, M. Bahout, A. B. Antunes, and G. Martinez, Bol. Soc. Esp. Ceram. Vidrio **47**, 143 (2008).

[103] J.-H. Chung, J.-H. Kim, S.-H. Lee, T. J. Sato, T. Suzuki, M. Katsumura, and T. Katsufuji, Phys. Rev. B **77**, 054412 (2008).

[104] B. Chardon and F. Vigneron, J. Magn. Magn. Mater. **58**, 128 (1986).

[105] A. Kuriki, Y. Moritomo, S. Xu, K. Ohoyama, K. Kato, and A. Nakamura, J. Phys. Soc. Jpn. **72**, 458 (2003).

[106] E. Jo, K. An, J. H. Shim, C. Kim, and S. Lee, Phys. Rev. B **84**, 174423 (2011).

[107] E. O. Wollan and W. C. Koehler, Phys. Rev. **100**, 545 (1955).

[108] R. G. Wyckoff, *Crystal Structures*, Vol. 1 (Interscience, New York, 1960).

[109] A. A. Bolzan, C. Fong, B. J. Kennedy, and C. J. Howard, Aust. J. Chem. **46**, 939 (1993).